

REPORT DOCUMENTATION PAGE

Form Approved
OMB No. 0704-0188

The public reporting burden for this collection of information is estimated to average 1 hour per response, including the time for reviewing instructions, searching existing data sources, gathering and maintaining the data needed, and completing and reviewing the collection of information. Send comments regarding this burden estimate or any other aspect of this collection of information, including suggestions for reducing the burden, to Department of Defense, Washington Headquarters Services, Directorate for Information Operations and Reports (0704-0188), 1215 Jefferson Davis Highway, Suite 1204, Arlington, VA 22202-4302. Respondents should be aware that notwithstanding any other provision of law, no person shall be subject to any penalty for failing to comply with a collection of information if it does not display a currently valid OMB control number.

PLEASE DO NOT RETURN YOUR FORM TO THE ABOVE ADDRESS.

1. REPORT DATE (DD-MM-YYYY) 12-04-2010			2. REPORT TYPE Final Technical Report		3. DATES COVERED (From - To) 17-06-2008 - 31-12-2009	
4. TITLE AND SUBTITLE Functional Epitaxial Oxide Devices					5a. CONTRACT NUMBER NA	
					5b. GRANT NUMBER N00014-08-1-1090	
					5c. PROGRAM ELEMENT NUMBER 0602271N or 0602114N	
6. AUTHOR(S) Leonard J. Brillson, John Volakis, and David C. Look					5d. PROJECT NUMBER NA	
					5e. TASK NUMBER NA	
					5f. WORK UNIT NUMBER NA	
7. PERFORMING ORGANIZATION NAME(S) AND ADDRESS(ES) David B. Doty, CRA, Associate Director, Engineering Experiment Station The Ohio State University 2070 Neil Avenue, Columbus, OH 43210 Telephone: (614) 292-8671, Fax: (614) 292-9615					8. PERFORMING ORGANIZATION REPORT NUMBER 1	
9. SPONSORING/MONITORING AGENCY NAME(S) AND ADDRESS(ES) Office of Naval Research, Attn: Ingham A. Mack, 875 North Randolph Street, Arlington, VA 22203-1995					10. SPONSOR/MONITOR'S ACRONYM(S) ONR	
					11. SPONSOR/MONITOR'S REPORT NUMBER(S) 1	
12. DISTRIBUTION/AVAILABILITY STATEMENT No restrictions						
13. SUPPLEMENTARY NOTES None						
14. ABSTRACT This report consists of three parts: an Ohio State Electrical & Computer Engineering /Physics component, an Ohio State Electrosciences component, and a Wright State component. This research effort addresses the need for high performance radio frequency (RF) components, specifically varactors and miniaturized, high gain, high bandwidth antennas. This program encompasses materials design, growth, processing, and physical characterization to develop varactor and antenna components with low dielectric loss. This program of research represents the second stage of the MultiFunctional oxide Materials, their Applications (MFMA) and devices initiative, which seeks to leverage Ohio strengths in oxide materials, magnetics and telecommunications into state-of-the-art electromagnetic technology that can revolutionize products in communications, sensors, and radar. Functional epitaxial oxide devices based on MFMA technology can enhance telecommunication (both wired and wireless, and optical), present-day computers, and provide technologies for nonvolatile data storage, sensors for defense and commercial application. This Ohio effort coordinates with complementary growth, characterization and device fabrication activities of Prof. Hedio Markey et al.						
15. SUBJECT TERMS RF componentry, multifunctional materials, complex oxides, epitaxial growth, antennas, varactors						
16. SECURITY CLASSIFICATION OF:			17. LIMITATION OF ABSTRACT UU	18. NUMBER OF PAGES 19	19a. NAME OF RESPONSIBLE PERSON Leonard J. Brillson	
a. REPORT U	b. ABSTRACT U	c. THIS PAGE U			19b. TELEPHONE NUMBER (Include area code) (614)-292-8015	

Final Report on Office of Naval Research Grant N00014-08-1-1090, “Functional Epitaxial Oxide Devices” – Principal Investigator: Leonard J. Brillson, co-Principal Investigators John Volakis and David C. Look

This report consists of three parts: an Ohio State Electrical & Computer Engineering /Physics component, an Ohio State Electrosiences component, and a Wright State component. This research effort addresses the need for high performance radio frequency (RF) components, specifically varactors and miniaturized, high gain, high bandwidth antennas. This program encompasses materials design, growth, processing, and physical characterization to develop varactor and antenna components with low dielectric loss. This program of research represents the second stage of the MultiFunctional oxide Materials, their Applications (MFMA) and devices initiative, which seeks to leverage Ohio strengths in oxide materials, magnetics and telecommunications into state-of-the-art electromagnetic technology that can revolutionize products in communications, sensors, and radar. Functional epitaxial oxide devices based on MFMA technology can enhance telecommunication (both wired and wireless, and optical), present-day computers, and provide technologies for nonvolatile data storage, sensors for defense and commercial application. This Ohio effort coordinates with complementary growth, characterization and device fabrication activities of Prof. Hadis Morkoc at Virginia Commonwealth University.

I. Electrical & Computer Engineering/Physics component of Ohio State Accomplishments

This component of the accomplishments centers on the materials growth, the characterization of their physical properties, and the design of processing techniques to minimize defects that increase dielectric loss, the major limitation to development of varactors and miniaturized, high gain, high bandwidth antennas. The materials used to develop these RF components are termed complex oxides, typically ceramic insulators such as SrTiO_3 , BaTiO_3 and BiFeO_3 with perovskite symmetry. The workhorse of complex oxides is SrTiO_3 , available in large area and widely used for epitaxial growth of other perovskites.

Depth-resolved cathodoluminescence spectroscopy (DRCLS) of atomically flat TiO_2 terminated SrTiO_3 single crystal surfaces reveals dramatic differences in native point defects produced by conventional etching with buffered HF (BHF) and an alternative procedure using HCl-HNO_3 acidic solution (HCLNO), which produces three times fewer oxygen vacancies before and nearly an order of magnitude fewer after pure oxygen annealing. See Figure 1. BHF-produced defect densities extend hundreds of nm below the surface, whereas the lower HCLNO-treated densities extend less than 50 nm. See Figure 2. This “Arkansas” HCLNO etch and anneal method avoids HF handling, providing high quality SrTiO_3 surfaces with low native defect density for complex oxide heterostructure growth. These measurements demonstrate that the conventional BHF etch creates high densities of oxygen vacancies that can be avoided by the alternative HCLNO etch. This is important since oxygen vacancies are known to be mobile and could in principle diffuse out of the SrTiO_3 “reservoir” into any epitaxial complex oxide overlayer and contribute free carriers to their transport properties.

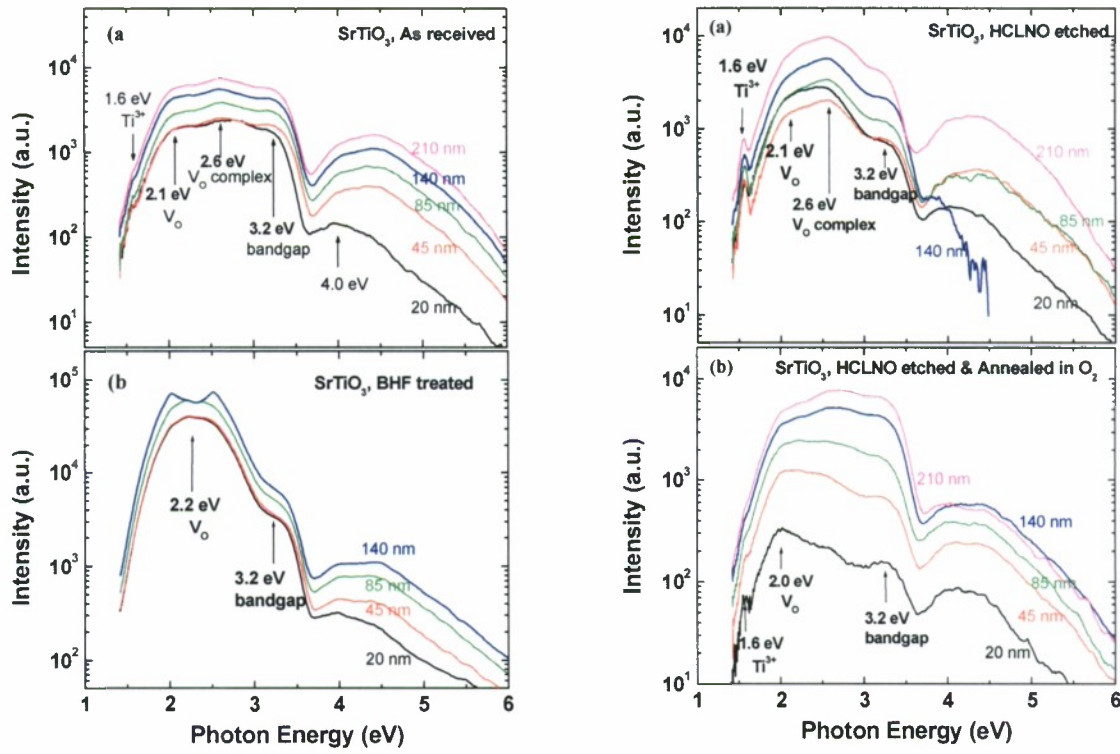


Figure 1. (Left) Representative CL spectra of an (a) As-received versus (b) BHF-treated SrTiO_3 single crystal. (Right) Representative CL spectra of a HCLNO treated SrTiO_3 single crystal (a) before and (b) after high temperature oxygen anneal.

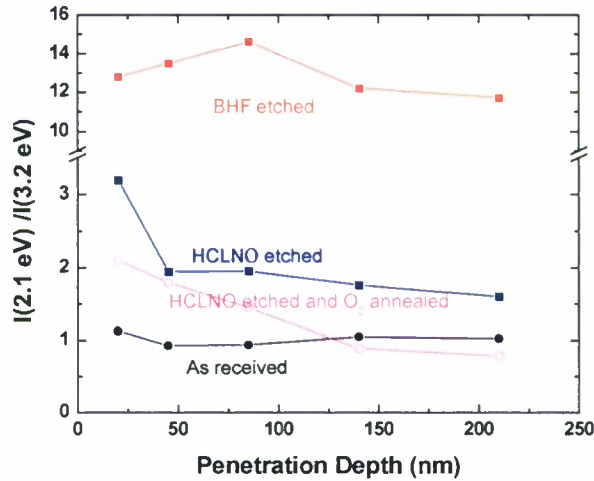


Figure 2. Intensity ratios of the deconvolved oxygen vacancy $I(2.1 \text{ eV}) + I(2.6 \text{ eV})$ to NBE (3.2 eV) emission features in the CL spectra of as-received and chemically-etched SrTiO_3 single crystals.

We used DRCLS to study the surface, bulk, and interface-localized electronic states in the band gap of epitaxial BiFeO_3 thin films. The BiFeO_3 films show a near band edge

emission at 2.7 eV and defect emissions at energies varying from 2.0 eV to 2.5 eV. See Figure 3. Figure 3(a) shows the strong variations in band gap (2.5 and 2.7 eV) and oxygen vacancy (2.0 and 2.2 eV) emissions that depend on growth method. Figure 3(b) shows how increasing Bi content produces higher oxygen vacancy densities. Figure 4 shows DRCL spectra for BiFeO₃ grown under compressive vs. tensile strain. The oxygen vacancy emission emerges with tensile vs. compressive strain, consistent with the suppression of these defects under compressive strain. The overall results clearly suggest that the electronic structure, especially the defect states and their spatial distributions, of BiFeO₃ films are strongly dependent on the growth conditions and method, stoichiometry and strain, so that understanding and controlling them are crucial to optimize BiFeO₃ film properties.

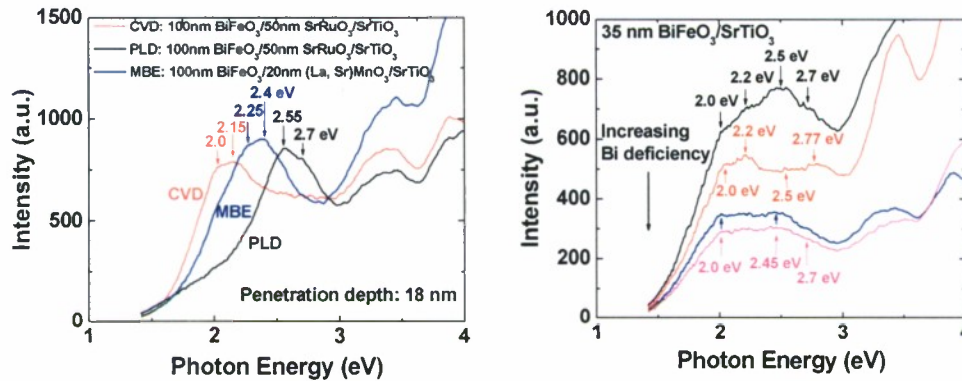


Figure 3. (a) CL spectra measured at a beam voltage of 1 kV for BiFeO₃ films grown by PLD, MBE and CVD. (b) CL spectra measured at a beam voltage of 1 kV (corresponding to a penetration depth of 18 nm) for Bi-deficient BiFeO₃ films grown by MBE.

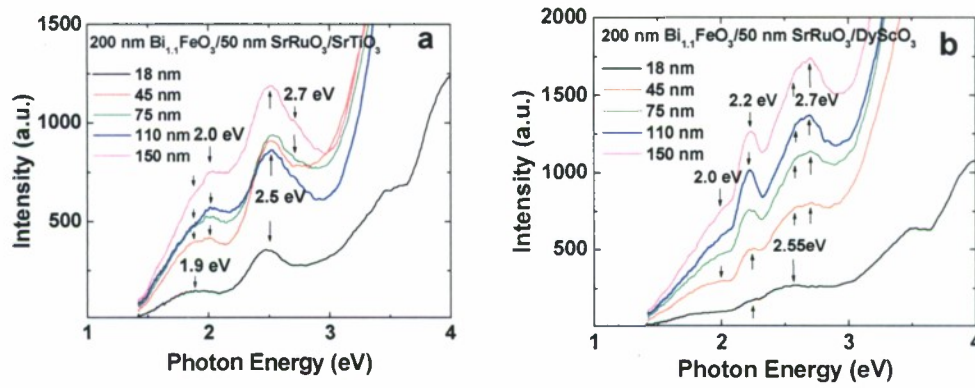


Figure 4. Depth resolved CL spectra of the PLD-grown BiFeO₃ films grown on different substrates: (a) SrTiO₃ (compressive strain) (b) DyScO₃ (tensile strain).

We used DCLS to study defects and their distributions in SrTiO₃ single crystals and epilayers. In SrTiO₃ single crystals, the dominant defects are oxygen vacancies that locate mainly near the free surface, while Ti interstitials locate further into the bulk. Vacuum annealing increases the density of oxygen vacancies at SrTiO₃ surfaces, but reduces the density of Ti interstitials located deeper. In epilayers, the density and distribution of the

defects depend on the film thickness and stoichiometry. The results reveal a strong dependence of SrTiO_3 native point defects and their depth distributions on epitaxial growth and process conditions.

The DRCLS results shown in Fig. 5 reveal dramatic differences between Sr_xTiO_3 epilayers of varying composition. In particular, the ratio of the V_O to near band edge emissions varies by over an order of magnitude between $x = 0.8$ and 1.2 . The V_O appears to increase with increasing Sr content. This may be related to formation of a partial $\text{Sr}_{n+1}\text{Ti}_n\text{O}_{3n+1}$ Ruddleson-Popper phase during growth without sufficient oxygen to maintain stoichiometry. Moreover, the defect peak ascribed to Ti^{3+} at 1.5 eV varies with stoichiometry as well - another indication that this feature is not impurity-related. This defect appears only for the Sr-deficient epilayers. Such a direct relationship between CL features and stoichiometry could be utilized to guide growth of stoichiometric SrTiO_3 as well as other complex oxides.

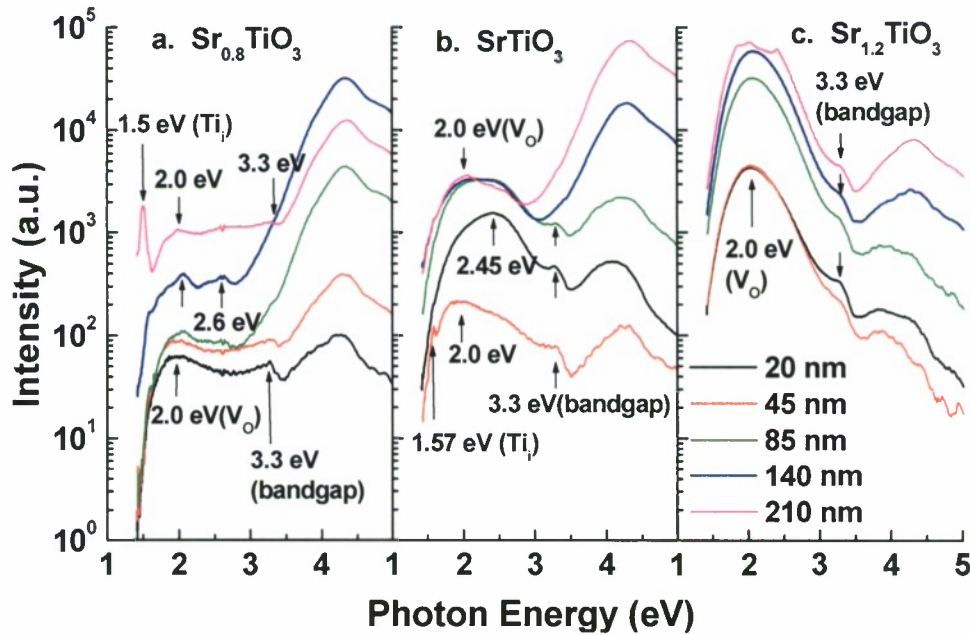


Figure 5. DRCLS spectra of Sr_xTiO_3 epilayers. a. $x=0.8$; b. $x=1.0$; c. $x=1.2$. With increasing Sr stoichiometry, the MBE-grown STO exhibits increasing oxygen vacancy (2.0 eV) densities.

In collaboration with Prof. Hadis Morkoc' group at Virginia Commonwealth University, we studied the structural and electrical properties of $\text{Ba}_{0.5}\text{Sr}_{0.5}\text{TiO}_3$ (BST) thin films prepared by off-axis RF magnetron sputtering with an oxygen mixing ratio ranging from 10% to 33% on MgO (001) substrates. Using DRCLS, we were able to observe defects in the films and their spatial distribution. See Figure 6. This paper shows that by reducing the oxygen vacancies one can increase the device tunability of BST films on MgO . The as-grow films showed high levels of oxygen vacancies, however after annealing in flowing oxygen these levels were reduced, while Ti related defect became more prevalent. It was also found that increasing the oxygen mixing ratio during growth

contributes to a further decrease of oxygen related defects and an increased device tunability of 8%.

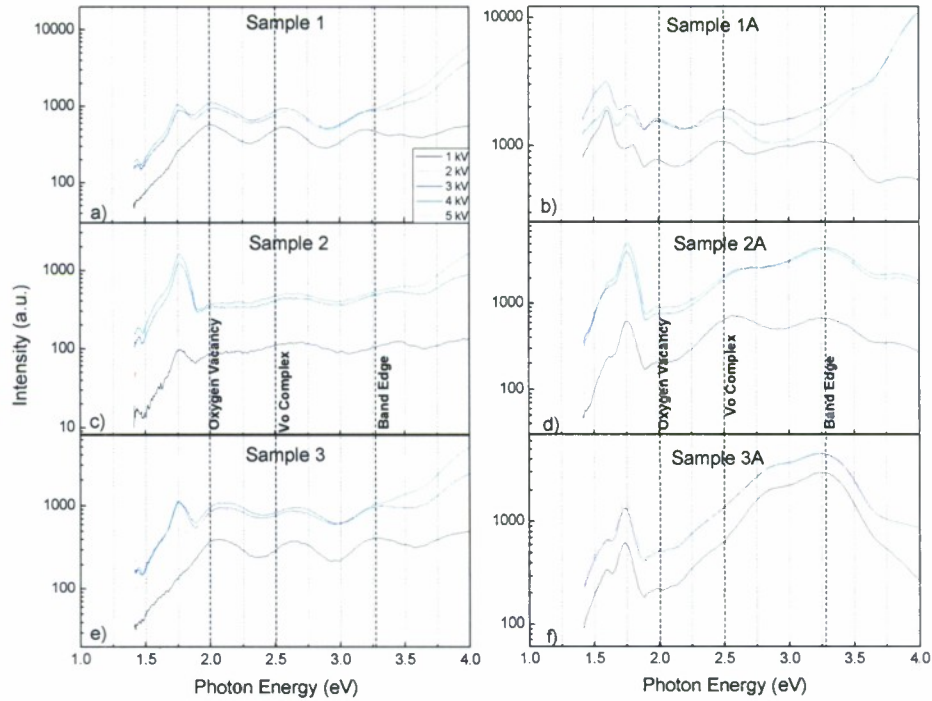


Figure 6. DRCLS showing oxygen vacancy peak at 2.0eV, V_O Complex at 2.5eV and BST near band edge peak at 3.26eV for a) as grown 10% oxygen mixing ratio (OMR), b) annealed 10% OMR, c) as grown 14% OMR, d) annealed 14% OMR, e) as grown 33% OMR, and f) annealed 33% OMR films.

Beyond characterization of complex oxides, we have commenced growing SrTiO₃ and BaTiO₃ epitaxial layers for RF varistors in collaboration with the Naval Research Laboratory (NRL) using our oxide MBE facility. Figure 7 DRCL spectra that, at near-surface probe depths, show near band edge emission (3.4 eV) that is very well defined and comparable to the oxygen vacancy emission (2.2 eV). Figure 7(b) shows the highest NBE quality ever observed in a perovskite. These results demonstrate that the epitaxial film surfaces are of high quality when grown using an oxygen plasma as the oxygen growth source vs. ambient oxygen. We are now growing similar samples of BST for fabrication into RF capacitors at NRL.

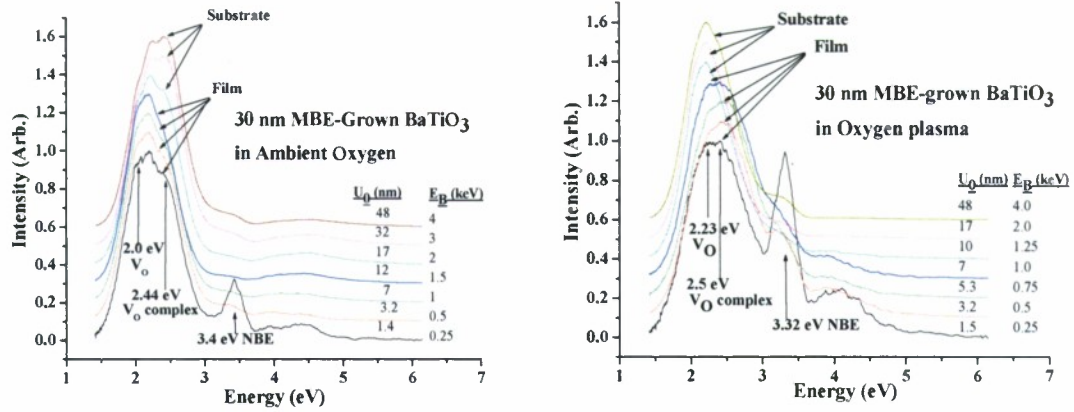


Figure 7. (a) DRCL spectra of 30 nm MBE-grown BaTiO_3 in ambient oxygen. Near band edge emission is much lower than defect emissions. (b) Grown in an oxygen plasma, near band edge emission grows substantially.

In order to optimize the growth of all these perovskites, we have assembled an analytical facility that links with the oxide MBE growth facility under ultrahigh vacuum (UHV) conditions. The linkage between these two facilities required in-house design and fabrication of components that are compatible with both sets of equipment. Thus the sample holder is compatible with the Continuous Angular Rotation (CAR) manipulator of the oxide MBE and retains good thermal contact with the CAR's heater. This sample holder can then be extracted under UHV for insertion into the facility for X-ray photoemission spectroscopy (XPS) and DRCLS. Hence we can grow epitaxial perovskite films and examine their chemical and electronic properties without exposing them to air. In turn, this allows us to modify and optimize the growth conditions *in-situ* in order to minimize native defects and optimize RF properties. Finally, this sets the stage for growing, characterizing, and optimizing the perovskite films envisioned for varactors and miniaturized, high gain, high bandwidth antennas.

II. Electrosiences Component of Ohio State Accomplishments

These accomplishments are centered primarily on (1) Magnetic Material characterization and (2) Magnetic Photonic antennas used to mitigate platform effects due to their more focused resonances. A portion of this work was supported by the Air Force Office of Scientific Research. Broadband Permeability Characterization of Thin and Small Magnetic Composites with Patterned Anisotropy

Characterization of Patterned Ferrite Films

An area of great need is that of measurement and characterization of antenna materials. Among numerous material characterization techniques, the resonant cavity method [1, 2] can measure in-plane permeability by aligning the sample's surface along the direction of the resonant mode polarization. However, in spite of its accuracy, the bandwidth of this method is highly restricted by the cavity resonant frequencies. The coil measurement method [3] is also popular, but its operation is limited to low frequencies (e.g., < 1 GHz). Typically, broadband characterization can be carried out using the transmission/reflection (T/R) method [4]. In this case, the material properties are de-embedded from the measured S -parameters with the material inserted into a transmission line (Tx-line).

To carry out accurate characterizations using the T/R method, it is necessary to design an appropriate Tx-line set-up that accommodates the given sample size, shape, magnetic properties, and frequency of interest. Herein, we employed a microstrip line structure to characterize the in-plane permeability of a patterned magnetic composite (see Fig. 8). Several microstrip line methods have been previously reported. A unique aspect of our work is the use of full-wave simulations to de-embed the permeability from the measured S -parameters. In the past, traditional quasi-static solutions were employed. This enables us to characterize a small piece of sample ($< 1 \text{ cm} \times 1 \text{ cm} \times 500 \text{ } \mu\text{m}$) over a broad bandwidth ($< 4.5 \text{ GHz}$).

Permeability De-embedding Process

The cross-section of the proposed microstrip line set-up is depicted in Fig. 9(a). A thin sample is laid on the surface of a holder. The sample is oriented to be illuminated by the H-field to realize in-plane permeability characterization. As can be seen, the H-field lines also interact with the air and holder. It is therefore necessary to de-embed the permeability of the sample from the surrounding effects.

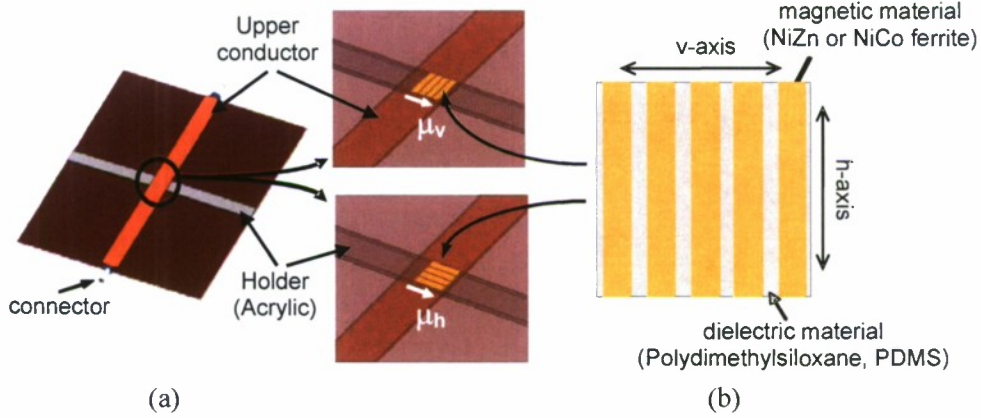


Fig. 8. Geometry of the measurement fixture and sample: (a) microstrip line structure, and (b) patterned magnetic composite. The insets to the right of (a) describe the in-plane anisotropy characterization by rotating the sample.

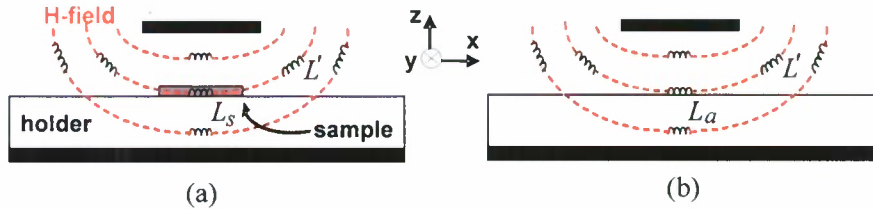


Fig. 9. Cross-section of the microstrip line set-up: (a) with sample, and (b) without sample.

Traditionally, the de-embedding process is designed using quasi-static analyses such as conformal mapping and variation methods. However, such quasi-static solutions are valid only when the sample is infinite along the x -direction (see Fig. 9). As our microstrip line

contains a sample of finite length in the x -direction, we proceeded to develop a de-embedding process based on full-wave simulation data.

For the new de-embedding process, a formulation that relates the permeability of the sample and the total permeability including all the H-field interactions (i.e., sample, holder and air) must first be developed. This can be done by approximating the H-field interactions by lump inductors. L_s denoted in Fig. 9(a) is the inductance of unit length along the sample. L_a in Fig. 9(b) also represents the inductance at the same location as L_s in absence of the sample. If we further assume that the H-field is not significantly perturbed by the thin and small sample, the total inductances from Fig. 9(a) and (b) is given by

$$\frac{1}{L_s^{tot}} - \frac{1}{L_a^{tot}} = \frac{1}{L_s + L'} - \frac{1}{L_a + L'}, \quad (1)$$

where L' is total series inductance connected with L_s or L_a along the same H-field line (see Fig. 9). As the inductance is proportional to permeability, the above may be re-written in terms of permeability values. Specifically, if we define (\square_{Rs} , \square_{Ra} , \square_{rs} , \square_{ra}) as the permeabilities correlates to (L_s^{tot} , L_a^{tot} , L_s , L_a), we can rewrite one as

$$\mu_{rs} = \frac{p_2 \mu_{Rs} - p_1 (1 + p_1) (1 + \mu_{Rs})}{p_2 \mu_{Rs} + (1 + p_1) (1 + \mu_{Rs})}, \quad (2)$$

where $p_1 = \frac{\mu_{rs} L'}{\mu_r' L_s} = \frac{\mu_{ra} L'}{\mu_r' L_a}$ and $p_2 = \frac{\mu_{rs} L_s^{tot}}{\mu_{Rs} L_s} = \frac{\mu_{ra} L_a^{tot}}{\mu_{Ra} L_a}$. Clearly, the above gives the

permeability of the sample (\square_{rs}) in terms of the total permeability (\square_{Rs}) and coefficients p_1 and p_2 . These coefficients are determined by curve fitting a set of \square_{Rs} and \square_{rs} data obtained from full-wave simulations.

Measurement Demonstration

To validate the proposed technique, two patterned ferrite composites were fabricated and characterized. These corresponded to NiZn-PDMS and NiCo-PDMS composites. The surface areas of these samples were 1 cm^2 , the thickness of the NiZn-PDMS sample was $610 \text{ }\mu\text{m}$ and that of NiCo was $480 \text{ }\mu\text{m}$. The samples were placed over a 1.25 mm thick Acrylic holder, and then inserted under a 14 mm wide upper conductor (see Fig. 8). The separation between the upper conductor and the ground was 3 mm .

Fig. 10(a) and (b) show the total permeability data for the NiZn and NiCo composites obtained directly from the measured S -parameters. These were extracted using the well-known Nicolson-Ross-Weir equations [4]. The insets at the bottom display the fabricated sample and direction of the applied H-field for each measurement. Overlaid with these total permeabilities are simulated curves (dotted lines), obtained from a full-wave simulation tool (Ansoft HFSS). \square_r values next to each curve denote the permeabilities of the sample assigned in the simulation. By curve fitting these simulated curves in a computer code (Matlab), the coefficients p_1 and p_2 were calculated.

Having obtained p_1 and p_2 , the sample permeabilities were calculated using Eq.(2). Fig. 11 illustrates the real part of permeability, $\text{Re}(\square_r)$, and magnetic loss-tangent, $\tan \square_r$, of the NiZn-PDMS composite. It is observed that the permeability and magnetic loss-

tangent are both reduced by introducing the patterning. Also, the results of the uniform sample measurements have good agreements to the results obtained from the Agilent E4991A impedance analyzer up to 1 GHz. It is worth noting that the impedance analyzer is only available below 1 GHz and not capable to characterize patterned structures with anisotropy. The de-embedded permeability values of the NiCo-PDMS showed the same trend as the NiZn-PDMS composite but not included in this paper.

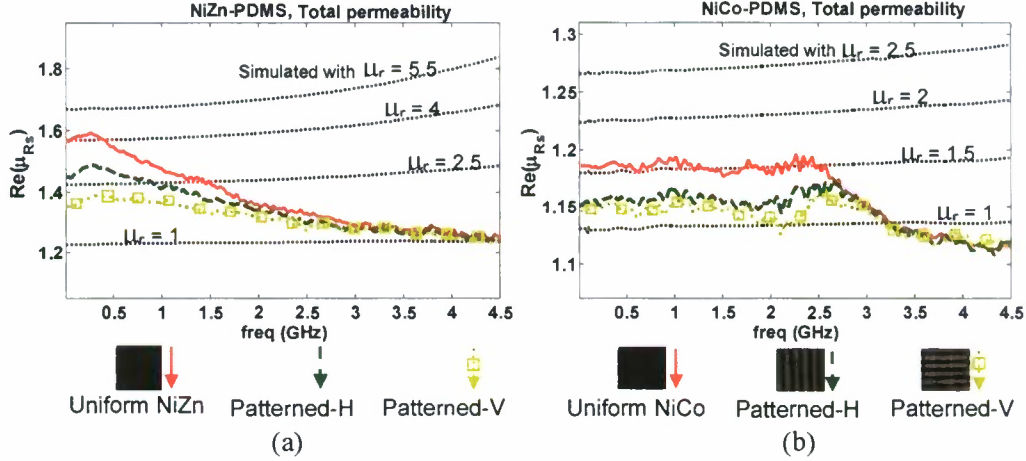


Fig. 10. Measured total permeabilities of (a) NiZn composite and (b) NiCo composite.

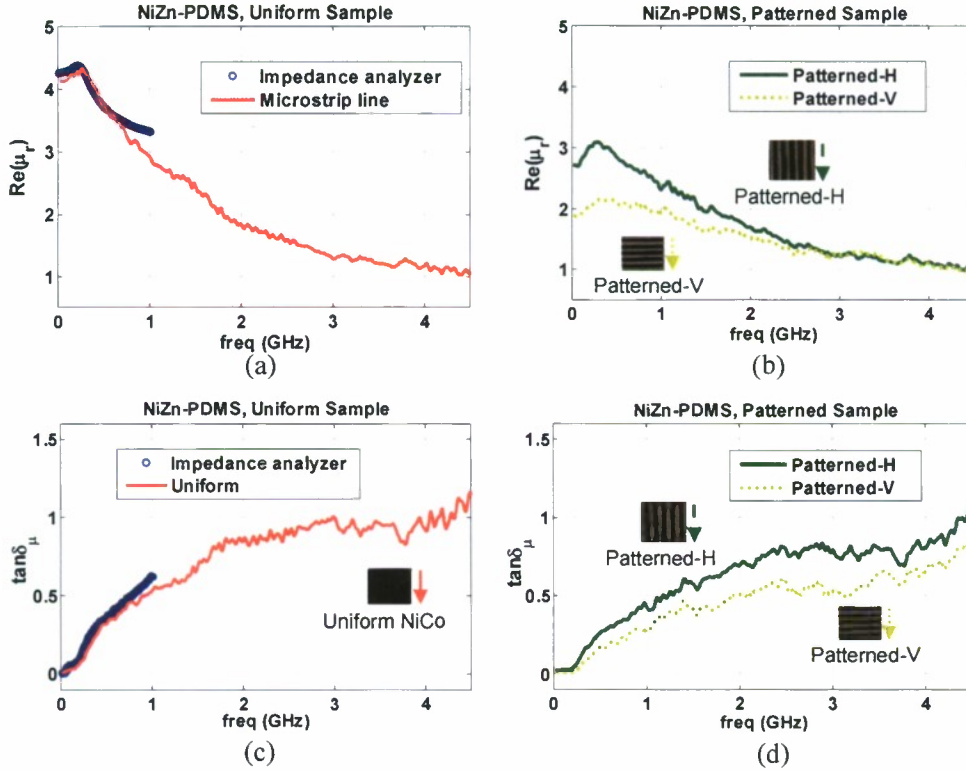


Fig. 11. Measured sample permeabilities of NiZn-PDMS composite: (a) $\text{Re}(\mu_r)$ of the uniform sample, (a) $\text{Re}(\mu_r)$ of the patterned sample, (c) $\tan\delta_\mu$ of the uniform sample, and (d) $\tan\delta_\mu$ of the patterned sample.

Comments

We described a microstrip line method for broadband characterization of the in-plane permeability. Unlike previously developed microstrip line methods, the proposed technique de-embeds the permeability values based on full wave simulations. Therefore, a large sample is no longer required as in conventional de-embedding processes using quasi-static analyses. The validity of the proposed technique was illustrated by measuring patterned magnetic composites with in-plane anisotropy up to 4.5 GHz.

References

- [1] R. M. Walser, "Metamaterials: An introduction," in *Introduction to complex mediums for optics and electromagnetic*, W. S. Weiglhofer *et al.*, Eds. Bellingham, WA: SPIE Press, 2003.
- [2] J. Krupka, and R. G. Geyer, "Complex permeability of demagnetized microwave ferrites near and above gyromagnetic resonance," *IEEE Trans. Magn.*, vol.32, pp.1924-1933, 1996.
- [3] Agilent Technologies, *Solutions for measuring permittivity and permeability with LCR meters and impedance analyzers*, Appl. Note 1369-1, 2003.
- [4] A. M. Nicolson and G. H. Ross, "Measurement of the intrinsic properties of materials by time domain techniques," *IEEE Trans. Instrum. Meas.*, vol. 19, pp. 377-382, 1970.

Ultrathin Miniature Antenna to Mitigate Platform Loading Effects

Introduction

In this effort, we introduce a cavity-backed (slot type) antenna that remains stable even when placed $1.5''$ ($\lambda_0/5$) away from vehicle edges. This is achieved by exploiting magnetic photonic crystals as in Fig. 8. These were discovered under the AFOSR MURI to have more confined resonances and do not diffract as much from the sides.

The modes depicted in Fig. 12 are termed as degenerate band edge (DBE) and magnetic photonic crystal (MPC) modes [1]-[3]. Small and highly directive antennas were already realized by harnessing these modes, leading to extreme wave slow down at much lower frequencies [4], [5]. More recently, the misaligned anisotropic dielectric layers in these volumetric crystals were successfully emulated using coupled transmission lines printed on uniform substrates as in Fig. 8(b). The DBE modes emulated using such coupled lines enabled smaller and high gain microstrip antennas [6]. Specifically, the maximally flat dispersion curves of the DBE crystals allowed for significant miniaturization over microstrip loop antennas, see Fig. 12(c). However, the zero slope associated with the $K = \pi$ resonance at the band edge suffers from reduced bandwidth. As a remedy, here we introduce biased ferrimagnetic inclusions under the coupled line sections to obtain nonreciprocal MPC dispersion modes. As depicted in Fig. 12(c), nonzero slope is realized in the dispersion curve around $K = \pi$ point. As the slope of the dispersion curve increases, bandwidth is increased. That is, bandwidth and wave velocity (or miniaturization) compete in our design. An advantage of the ferrimagnetic inclusions is the possibility to fine tune or retune the antenna after installation.

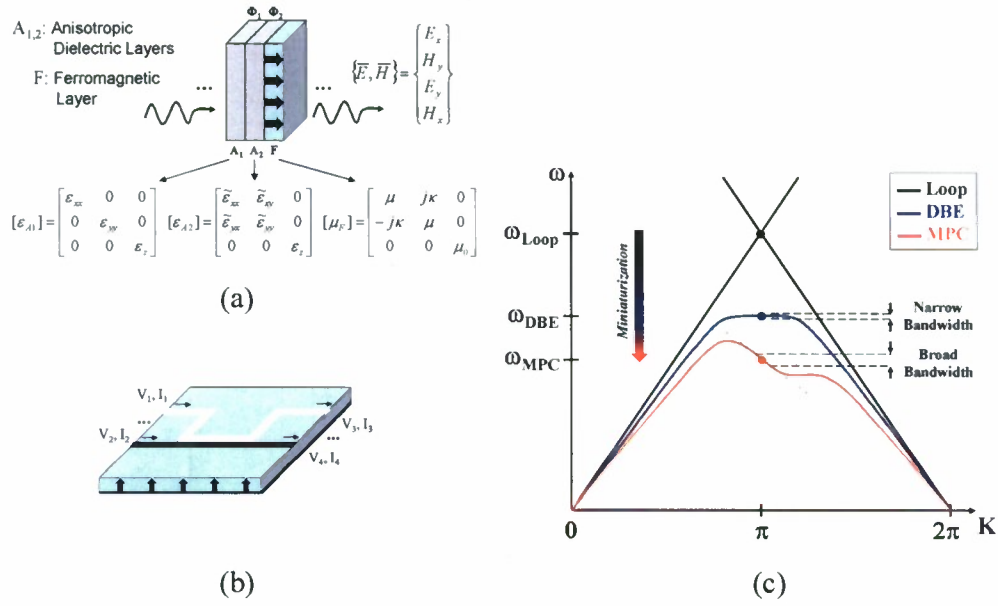


Figure 12: (a) Volumetric MPC unit cell. (b) Emulation of anisotropy using uncoupled and coupled microstrip lines. (c) DBE and MPC dispersion curves.

MPC Antenna Design and Performance

DBE dispersion modes were previously emulated in [6] using uncoupled and coupled lines on a uniform dielectric substrate. A design is given in 9(a)-top. Inclusion of ferrimagnetic pucks under the coupled transmission line sections (as in Fig. 13(a)-bottom) leads to MPC modes, see Fig. 13(b). The latter are associated with increased bandwidth [7]. Next, the MPC antenna was formed by circularly cascading two unit cells, as illustrated in Fig. 13(c).

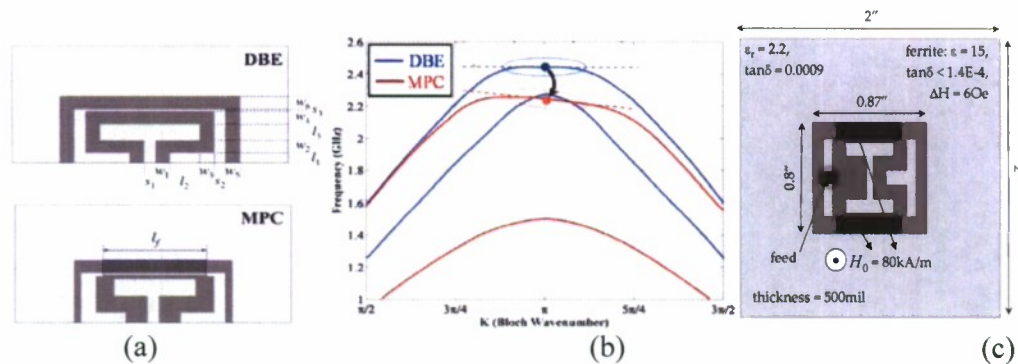


Figure 13: (a) DBE and MPC unit cell geometries. (b) DBE and MPC dispersion diagrams. (c) Resonant MPC antenna formed by circularly cascading two unit cells.

The developed MPC antenna in Fig. 13 was compared to a standard patch antenna on a 2"x2" ground plane. This comparison was intended to assess performance improvement over patch antennas. We found that the patch antenna had to be of size 1.23"x1.14" (to

resonate at 2.35 GHz) and delivered 11.6% bandwidth and 6.7 dB gain. In contrast, the MPC antenna achieved 8.8% bandwidth and 6.2 dB gain but needed a footprint of only 0.8"x0.87". That is, the MPC antenna used here was %50 smaller as compared to a patch. In the next section, this MPC antenna is redesigned using a cavity-backed configuration. As such, it can be recessed into the platform. We then proceed to evaluate antenna effects due to various platform sizes.

Cavity-Backed and Recessed MPC Antenna

In designing a cavity-backed MPC, we first considered a smaller, 1.5"x1.5"x0.5" substrate without any cavity and investigated the cases where the antenna is placed on ground planes of various sizes. As observed from Fig. 14(a), antennas with ground planes at least larger than 3"x3" have good impedance matching around 2.42 GHz. However, the isolated (stand-alone) MPC antenna on a 1.5"x1.5" ground plane (i.e., as large as its substrate) shifts its resonance down to 2.36 GHz. This detuning was decreased significantly by placing the MPC antenna in a metallic cavity that minimizes interactions with the ground plane, as illustrated in Fig. 14(b). But, although platform effects were suppressed, the cavity-backed MPC had its resonance increased to 2.44 GHz and antenna bandwidths were diminished.

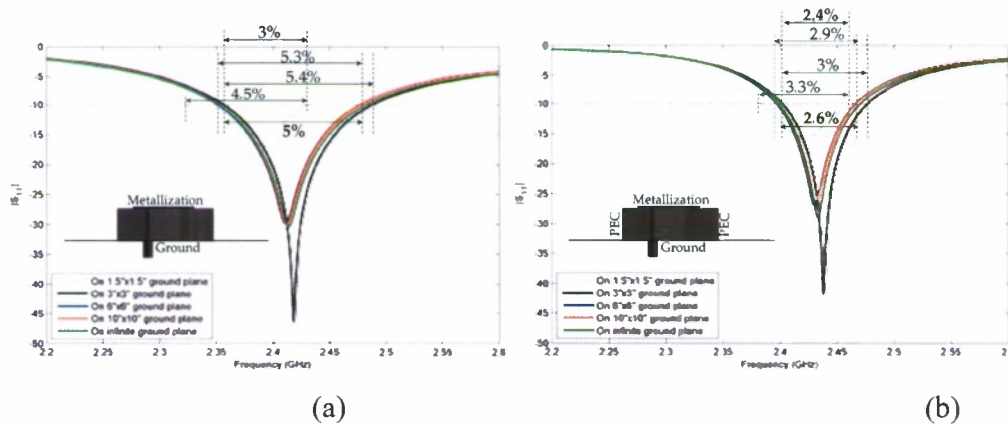


Figure 14: (a) Return losses of MPC antennas placed on a ground plane, (b) Return losses of cavity-backed MPC antennas placed on a ground plane.

Although the cavity-backed antenna configuration in Fig. 14(b) is useful for mitigating platform loading effects, it is still protruding. In fact, the cavity-backed design also allows recessing the MPC antenna under the ground plane without significant degradation in performance, see Fig. 15(a). Thus, a small and zero-profile aperture was created on the ground plane. This slightly shifted the antenna resonances to around 2.45 GHz, without deteriorating their bandwidths. In addition to mitigating platform effects with the cavity-backed design, the ferrimagnetic blocks inside the MPC antenna could be further used for tuning the resonance by changing the magnetic bias strength. This is illustrated in Fig. 15(b), where all antennas are retuned to resonate at 2.45 GHz. In this case, any detuning due to different ground plane sizes is completely eliminated.

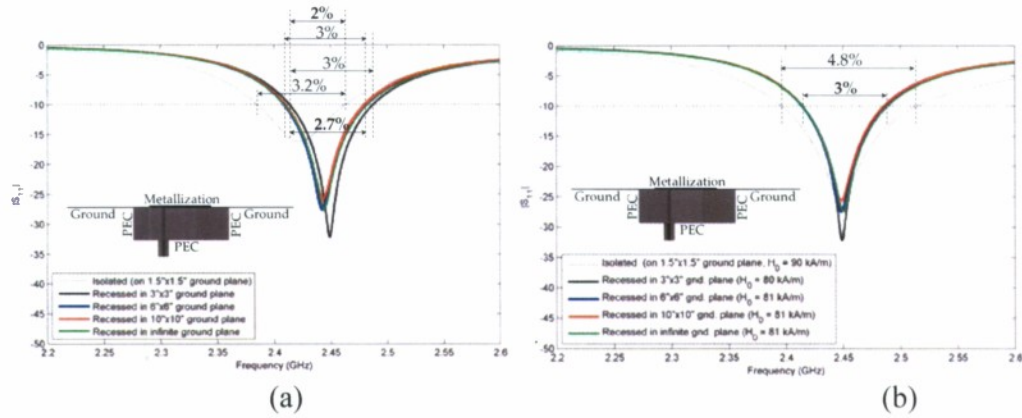


Figure 15: (a) Return losses of cavity-backed MPC antennas recessed into a ground plane, (b) Return losses of cavity-backed and recessed MPC antennas after retuning.

Finally, Fig. 16 shows the radiation patterns of cavity-backed and recessed MPC antennas in Fig. 15(a). Broadside radiation patterns are retained almost the same. The main differences are observed in back lobes, which are small. Additional effort is currently pursued to evaluate MPC antenna patterns for various locations on vehicular platforms and carry out optimizations.

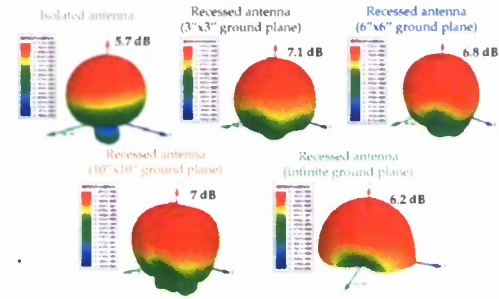


Figure 16: Radiation patterns of the cavity-backed and recessed MPC antennas (without any retuning).

References

- [1] A. Figotin and I. Vitebsky, "Nonreciprocal magnetic photonic crystals," *Phys. Rev. E*, vol. 63, pp. 066 609–066 625, Feb. 2001.
- [2] A. Figotin and I. Vitebsky, "Frozen light in photonic crystals with degenerate band edge," *Phys. Rev. E*, vol. 74–066613, pp. 1–17, Oct. 2006.
- [3] A. Figotin and I. Vitebsky, "Slow-wave resonance in periodic stacks of anisotropic layers," *Phys. Rev. E*, vol. 76–053839, pp. 1–12, Nov. 2007.
- [4] G. Mumcu, K. Sertel, and J. L. Volakis, "Miniature antennas and arrays embedded within magnetic photonic crystals," *IEEE Antennas Wireless Propag. Lett.*, vol. 5, pp. 168–171, Dec. 2006.
- [5] S. Yarga, G. Mumcu, K. Sertel, and J. L. Volakis, "Degenerate band edge crystals and periodic assemblies for antenna applications," in *Proc. IEEE Int. Workshop on Antenna Technol. Small Antennas and Novel Metamater.*, Mar. 2006, pp. 408–411.
- [6] G. Mumcu, K. Sertel, and J. L. Volakis, "Miniature antenna using printed coupled lines emulating degenerate band edge crystals," *IEEE Trans. Antennas Propag.*, vol. 57, no. 6, pp. 1618–1624, June 2009.
- [7] E. Irci, K. Sertel, and J. L. Volakis, "Antenna miniaturization using coupled microstrip lines emulating magnetic photonic crystals," in *Proc. 2009 IEEE Antennas and Propagation Soc. Int. Symp.*, pp. 1–4.

III. Summary of Wright State accomplishments in 1st year

In the first year of this program, we carried out Hall-effect and low-T photoluminescence spectroscopy (PL) measurements on bulk (100) and (110) SrTiO₃ purchased from MTI Corp. This material was semi-insulating, and measurements in the dark yielded no useful parameters. Under white-light irradiation, we measured resistivity of $\sim 10^9 \Omega\text{-cm}$ and mobility $\sim 500 \text{ cm}^2/\text{V-s}$. Low-T PL produced a strong feature at 2.54 eV. This line is reminiscent of the green band in ZnO, which has been attributed to the O vacancy, among other things and is consistent with oxygen vacancy complexes attributed to this band elsewhere.

We performed 1-MeV electron irradiation on the SrTiO₃ substrate materials. The idea here was to look for a conductivity increase which might indicate that O vacancies were shallow donors, a standard (but possibly wrong) assumption in the oxide community. The sample remained semi-insulating, suggesting that either the O vacancy (V_O) is not a shallow donor, or that the O Frenkel pairs produced by the irradiation immediately annihilate.

We performed 4-keV Ar-ion bombardment on the SrTiO₃ substrate materials. This technique had been earlier shown to increase the conductance in SrTiO₃, and our data indeed confirmed this result. Applying conventional wisdom, the increase in conductance was thought to be due to the production of V_O centers; however, as was the case with the electron irradiation, the increase in conductance was too small to be practical.

We purchased a SrTiO₃ target for pulsed-laser deposition (PLD) growth of homoepitaxial SrTiO₃, also heteroepitaxial SrTiO₃ growth on sapphire, and in collaboration with Dr. Kevin Leedy of AFRL/RYS, grew the latter. Both homoepitaxial and heteroepitaxial PLD growths turned out to be semi-insulating.

Wright State Accomplishments in 2nd year

Thin-film growth - At the end of the first year we had not accomplished one of our major goals, namely, to produce SrTiO₃ with a wide range of conductivity, from semi-insulating to highly conductive. Neither electron irradiation nor Ar-ion bombardment of commercial SrTiO₃ crystals seemed to be effective. Furthermore, from literature studies, we expected that growing conductive thin films by PLD, a technique that was available in our laboratory, could be accomplished only by using a very low O₂ background pressure P_{O2}, and unfortunately the resulting Zn-rich growth resulted in Zn-coated observation windows. Thus, we decided to try a different tack: (1) use a SrTiO₃ target doped with a donor element, Nb; and (2) do a post-growth anneal in vacuum. Indeed, this technique worked very well, and enabled the growth of n-type material having a wide range of resistivities, 10^7 to $10^{-1} \Omega \text{ cm}$. Table I summarizes the results. The thicknesses are about 0.2 μm in all cases except for that of sample STO-Nb-1A, which is about 0.5 μm .

Temperature-dependent Hall-effect measurements - We will concentrate here on our most conductive sample, STO-Nb-2, which was Nb-doped and annealed in vacuum, having a room-temperature resistivity of $0.18 \Omega\text{-cm}$, a mobility of $0.11 \text{ cm}^2/\text{V-s}$, and an electron concentration of $3.0 \times 10^{20} \text{ cm}^{-3}$. The temperature dependences of resistivity, mobility, and carrier concentration are plotted in Figures 17, 18, and 19, respectively. Note that the resistivity ρ curve is smooth, while the mobility μ and concentration n

curves are noisy, even after smoothing, and seem to show drift or instability. The reason is that μ is very low, and thus the Hall voltage is very low and can be greatly influenced by noise fluctuations. The low-temperature behavior of n , Fig. 19, is somewhat ambiguous because of the noise and instability issues, but is likely rather flat, in reality. Such flatness has been observed many times in many different semiconductor materials, and is often indication of a surface or interface layer of high degeneracy.

Table I. Growth of SrTiO₃ by PLD and control of conductivity by annealing

Sample	P _{O₂,growth}	T _{growth}	Doping	Pre-deposit anneal	Post-deposit anneal	Internal anneal	External anneal			
STO-Nb-2	1 mTorr	660 °C	Nb	660°C, 1mT O ₂ , 60min	550°C, 600T O ₂ , 60min	800°C, vac, 60min	none			
STO-Nb-1A	30 mTorr	660 °C	Nb	660°C, 30mT O ₂ , 60min	550°C, 600T O ₂ , 60min	800°C, vac, 60min	none			
STO-4B-1	75 mTorr	620 °C	none	none	550°C, 600T O ₂ , 120min	800°C, vac, 60min	none			
STO-4B-3	75 mTorr	620 °C	none	none	550°C, 600T O ₂ , 120min	800°C, vac, 60min	300°C, O ₂ , 30min			
STO-4B-4	75 mTorr	620 °C	none	none	550°C, 600T O ₂ , 120min	800°C, vac, 60min	350°C, O ₂ , 30min			
STO-4B-5	75 mTorr	620 °C	none	none	550°C, 600T O ₂ , 120min	800°C, vac, 60min	400°C, O ₂ , 30min			
STO-4B-6	75 mTorr	620 °C	none	none	550°C, 600T O ₂ , 120min	800°C, vac, 60min	450°C, O ₂ , 30min			
STO-4B-2	75 mTorr	620 °C	none	none	550°C, 600T O ₂ , 120min	800°C, vac, 60min	500°C, O ₂ , 30min			
Sample				ρ (Ω -cm)	μ (cm ² /V-s)	n (cm ⁻³)				
STO-Nb-2				0.18	0.11	3.0×10^{20}				
STO-Nb-1A				1.1	0.34	1.7×10^{19}				
STO-4B-1				1.8	0.58	6.0×10^{18}				
STO-4B-3				5.1	0.28	4.5×10^{18}				
STO-4B-4				9.9	0.29	2.1×10^{18}				
STO-4B-5				4.0×10^1	0.34	4.5×10^{17}				
STO-4B-6				1.7×10^3	0.78	4.6×10^{15}				
STO-4B-2				$> 10^7$?	2×10^{10}				

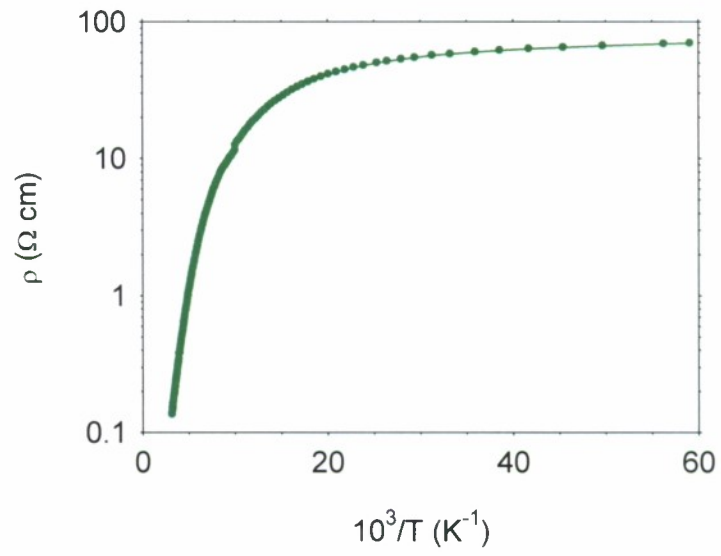


Figure 17. Resistivity ρ vs inverse temperature for SrTiO_3 sample STO-Nb-2

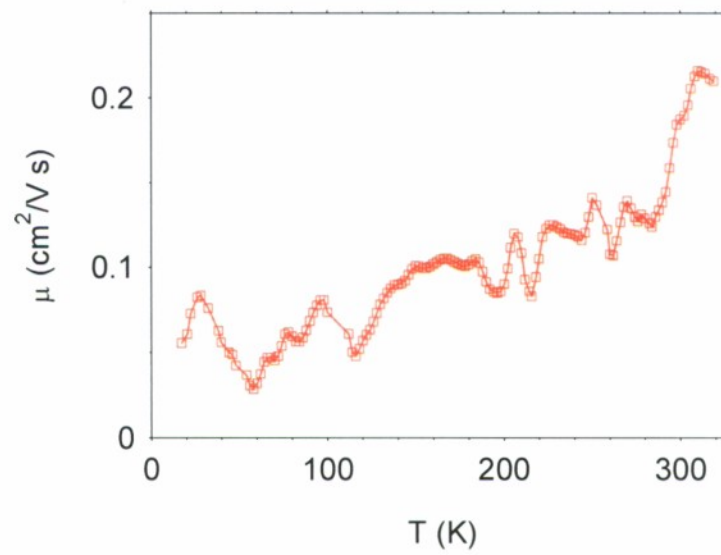


Figure 18. Mobility μ vs temperature for SrTiO_3 sample STO-Nb-2

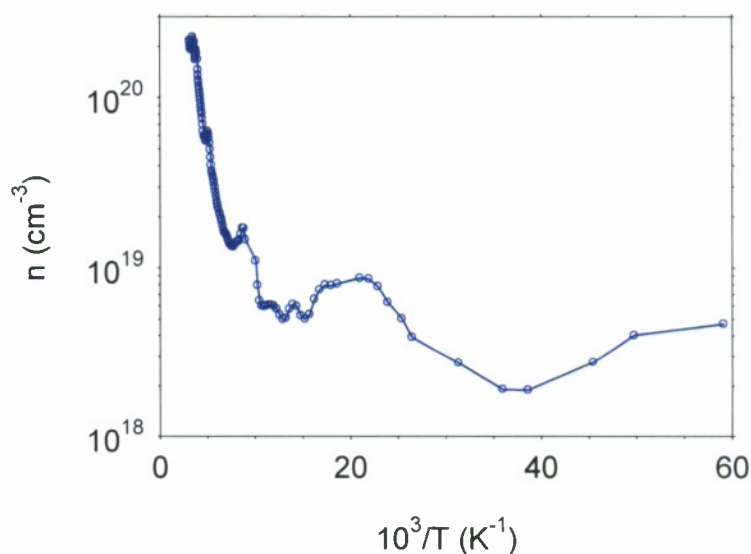


Figure 19. Electron concentration n vs inverse temperature for SrTiO_3 sample STO-Nb-2

At higher temperatures, n seems to be activated, with an activation energy of about 70 meV. The mobility μ , Fig. 18, increases with temperature, indicative of ionized-impurity or ionized-defect scattering. Such a mechanism leads to a $T^{3/2}$ variation in a nondegenerate material, but this material is partially degenerate so the temperature dependence is weakened. The resistivity, Fig. 17, is also quite flat at low temperatures, again likely showing the presence of a degenerate surface or interface layer, and then ρ becomes activated at higher temperatures. The resistivity activation energy is about 100 meV, somewhat larger than that of the concentration because ρ involves both n and μ . The conclusion of all of these data is that the sample contains a shallow donor of very high concentration, well over 10^{20} cm^{-3} , and its activation energy E_D at this concentration is about 70 meV. Of course, at lower concentrations, E_D would be higher, because the screening effects would be weaker. The identity of this donor will require more detailed studies, but optical measurements give some clues.

Photoluminescence (WSU) and cathodoluminescence (OSU) measurements -

Photoluminescence (PL) measurements in SrTiO_3 are difficult, because the lines tend to be broad and the intensities relatively weak, especially for thin layers such as these, and weak pump powers, of a few W/cm^2 . Indeed, in measurements of bulk materials, the only prominent PL line is a green band at about 2.5 eV. This band along with two others at 2.9 and 3.2 eV were carefully studied by S. Mochizuki et al, J. Phys.: Condens. Matter 17, 923 – 948, 2005, and the 2.5-eV band was attributed to oxygen defects, in particular $\text{Ti}^{3+}\text{-V}_\text{O}$ centers in the surface region. While our PL measurements yielded little on these samples, some cathodoluminescence (CL) measurements by M. Rutkowski, K. McNicholas, S. Shen, and L. Brillson at OSU gave much better results and will be discussed in more detail by those co-workers. Their band at 2.56 eV is indeed by far the most prominent feature in sample STO-Nb-2 when their exciting electron beam has a

voltage of 0.5 kV, but then decreases strongly relatively to the other features for beam voltages of 1 and 2 kV. These comparisons suggest that it is surface-related. It is also less prominent in the more resistive samples, which is consistent with it being donor-related. Finally, broad bands near 2.5 eV are often seen in oxide semiconductors, and generally they are assigned to O vacancies. Thus, although none of this evidence is totally conclusive, it is reasonable to assign the 2.5-eV feature to an O-vacancy-related defect near the surface, as surmised by Mochizuki et al. Further studies will be necessary to fully understand the impurities and defects that contribute to the electrical and optical properties of SrTiO₃, but some advances have been realized in the 2nd year of this project.

Publications

1. A.J. Hauser, J. Zhang, L. Mier, R.A. Ricciardo, P.M. Woodward, T.L. Gustafson, L.J. Brillson, and F.Y. Yang, "Characterization of electronic structure and defect states of thin epitaxial BiFeO₃ films by UV-Vis absorption and cathodoluminescence spectroscopies," *Appl. Phys. Lett.* 92, 222901(2008).
2. J. Zhang, S. Walsh, C. Brooks, D.G. Schlom, and L.J. Brillson, "Depth-resolved cathodoluminescence spectroscopy study of defects in SrTiO₃," *J. Vac. Sci. Technol. B* 26, 1466 (2008).
3. J. Zhang, J. Chakhalian, M. Kareev, J. Liu, S. Prosandeev, and L.J. Brillson, "Depth-Resolved Subsurface Defects in Chemically Etched SrTiO₃," *Appl. Phys. Lett.* 94, 092904 (2009).
4. J. Zhang, M. Rutkowski, L.W. Martin, T. Conry, R. Ramesh, J.F. Ihlefeld, A. Melville, D.G. Schlom, and L.J. Brillson, "Surface, Bulk and Interface Electronic States of Epitaxial BiFeO₃," *J. Vac. Sci. Technol. B*, 27, 2012-2014 (2009).
5. M. Rutkowski, A.J. Hauser, F.Y. Yang, R. Ricciardo, T. Meyer, P.M. Woodward, A. Holcombe, P. Morris, and L.J. Brillson, "X-Ray Photoemission Spectroscopy of Sr₂FeMoO₆ Film Stoichiometry and Valence State," *J. Vac. Sci. Technol.*, submitted.
6. Emmanuel Rowe, Bo Xiao, Vitaliy Avrutin, Ümit Özgür and Hadis Morkoç, Jun Zhang and L.J. Brillson, S. W. Kirchoefer, L. M. B. Alldredge, W. Chang, and J. M. Pond, "Effects of oxygen mixing ratio on device tunability and point defect distribution in sputtered Ba_{0.5}Sr_{0.5}TiO₃ on MgO," *Appl. Phys. Lett.*, submitted.
7. Nil Apaydin, G. Mumcu, E. Irci, K. Sertel and J.L. Volakis, "Miniature Antennas Based on Printed Coupled Lines Emulating Anisotropy," to appear in *IET Microwaves*.
8. E. Irci, K. Sertel and J.L. Volakis, "Antenna Miniaturization for Vehicular Platforms Using Printed Coupled Lines Emulating Magnetic Photonic Crystals," to appear in *Special Metamaterials issue ELSEVIER*, 2010.
9. Jae-Young Chung, Kubilay Sertel, and John L. Volakis, "A Non-invasive metamaterial characterization system using synthetic Gaussian aperture," *IEEE Trans. Antennas Propagat.*, vol. 57, no. 7, pp. 2006-2013, July, 2009.

Presentations

1. "Cathodoluminescence Spectroscopy Studies of Band Gap and Defects of Epitaxial BiFeO₃ Films," J. Zhang, A.J. Hauser, L. Mier, R. Ricciardo, P.M.

- Woodward, T. L. Gustafson, F.Y. Yang, and L.J.Brillson, 50th Annual Electronic Materials Conference, Santa Barbara, CA, June 26, 2008.
2. "Nanoscale Depth-Resolved Study of Point Defects at Chemically-Etched SrTiO₃ Crystal Surfaces," L.J. Brillson, J. Zhang, M. Kareev, J. Liu, and J. Chakhalian, 15th International Workshop on Oxide Electronics, Estes Park, CO, September 16, 2008.
 3. "Nanoscale Depth-Resolved Study of Point Defects at Chemically-Etched SrTiO₃ Crystal Surfaces," J. Zhang, M. Kareev, J. Liu, J. Chakhalian, and L.J. Brillson, 36th International Conference on the Physics and Chemistry of Surfaces and Interfaces, Santa Barbara, CA, January 13, 2009.
 4. "Surface, Bulk and Interface Electronic States of Epitaxial BiFeO₃ Films," J. Zhang, M. Rutkowski, L.J. Brillson, L. Martin, T. Conry, R. Ramesh, J.F. Ihlefeld, A. Melville, and D.G. Schlom, 36th International Conference on the Physics and Chemistry of Surfaces and Interfaces, Santa Barbara, CA, January 13, 2009.
 5. "Impact of Growth Process on Native Point Defects and Correlation with Dielectric Properties of Barium Strontium Titanate," M. Rutkowski, J. Zhang, D.R. Douth, L.J. Brillson, L.M.B. Alldredge, W. Chang, and S.W. Kirchoefer, 2009 Electronic Materials Conference, University Park, PA, June 25, 2009.
 6. E. Irci, K. Sertel, and J.L. Volakis, "Antenna Miniaturization Using Coupled Microstrip Lines Emulating Magnetic Photonic Crystals," 2009 IEEE Antennas and Propagation Society Symposium, Charleston, SC, June 2009.
 7. N. Apaydin, K. Sertel, J. L. Volakis, "3-D Artificial Media Exhibiting Degenerate Band Edge and Frozen Modes", APS, Session 502, Charleston, SC., 2009.
 8. E. Irci, K. Sertel and J.L. Volakis, "Ultrathin Miniature Antenna to Mitigate Platform Loading Effects," 2010 IEEE Antennas and Propagat. Symposium, Toronto, Canada.
 9. Nil Apaydin*, Kubilay Sertel, and John L. Volakis, "Demonstration of Unidirectional Printed Structures Emulating Magnetic Photonic Crystals," 2010 IEEE Antennas and Propagat. Symposium, Toronto, Canada.